



The beneficial use of non-thermal plasma in synthesis of Ni/Al₂O₃–MgO nanocatalyst used in hydrogen production from reforming of CH₄/CO₂ greenhouse gases

Pooya Estifaei^{a,b}, Mohammad Haghighi^{a,b,*}, Ali Akbar Babaluo^{a,c}, Nader Rahemi^{a,b}, Mahdi Fallah Jafari^d

^a Chemical Engineering Faculty, Sahand University of Technology, P.O. Box 51335-1996, Sahand New Town, Tabriz, Iran

^b Reactor and Catalysis Research Center (RCRC), Sahand University of Technology, P.O. Box 51335-1996, Sahand New Town, Tabriz, Iran

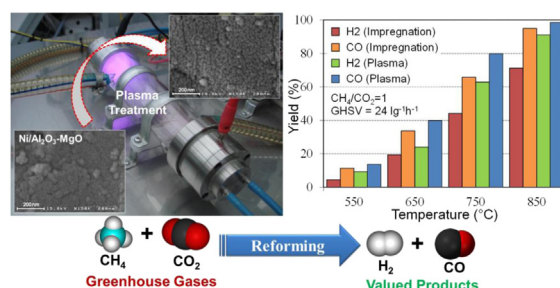
^c Nanostructure Material Research Center (NMRC), Sahand University of Technology, P.O. Box 51335-1996, Sahand New Town, Tabriz, Iran

^d National Iranian Oil Refining & Distribution Company (NIORDC), National Iranian Oil Company (NIOC), P.O. Box 15815-3499, Tehran, Iran

HIGHLIGHTS

- Successful treatment of Ni/Al₂O₃–MgO nanocatalyst with glow discharge plasma.
- Formation of small and highly dispersed NiO crystals in plasma Ni/Al₂O₃–MgO catalyst.
- Uniform and agglomeration free morphology for plasma Ni/Al₂O₃–MgO catalyst.
- More reactivity and stability for plasma treated Ni/Al₂O₃–MgO catalyst in dry reforming of CH₄.
- Getting H₂/CO very close to 1 at high temperatures over plasma treated Ni/Al₂O₃–MgO catalyst.

GRAPHICAL ABSTRACT



ARTICLE INFO

Article history:

Received 17 November 2013

Received in revised form

10 January 2014

Accepted 28 January 2014

Available online 12 February 2014

Keywords:

Dry reforming

Methane

Synthetic gas

Nanocatalyst

Non-thermal plasma

ABSTRACT

In our continuing effort to investigate the effect of non-thermal plasma on CH₄/CO₂ reforming catalysts, Ni/Al₂O₃–MgO nanocatalyst is investigated. The impregnated and plasma treated nanocatalysts are characterized using XRD, FESEM, TEM, EDX Dot-Mapping, BET, TG–DTG, XPS and FTIR techniques. XRD patterns show high dispersion and strong interaction of active phase. FESEM images display smaller particle size and a narrow particle size distribution for plasma treated sample. According to the BET analysis, the calculated surface area of plasma treated sample is 11% higher. TEM images show particles of active phase are fairly small and well-dispersed as a result of plasma treatment. In addition to better structural and physicochemical properties, the Ni/Al₂O₃–MgO nanocatalyst which treated by non-thermal plasma has higher activity and significant anti-coke properties in the CH₄/CO₂ reforming reaction at 550–850 °C temperature range using a mixture of CH₄:CO₂ = 0.5–2.

© 2014 Elsevier B.V. All rights reserved.

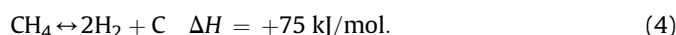
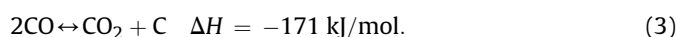
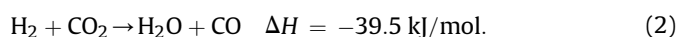
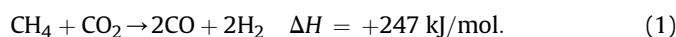
* Corresponding author. Reactor and Catalysis Research Center, Sahand University of Technology, P.O. Box 51335-1996, Sahand New Town, Tabriz, Iran. Tel.: +98 411 3458096, +98 411 3459152; fax: +98 411 3444355.

E-mail address: haghighi@sut.ac.ir (M. Haghighi).

URL: <http://rcrc.sut.ac.ir>

1. Introduction

During the past decade, reforming of CH_4/CO_2 or dry reforming of methane (DRM) has attracted attentions because of its high potential in syngas (mixture of CO and H_2) production, using two greenhouse gasses (CO_2 and CH_4) as feedstock and also producing syngas with H_2/CO ratio close to 1 [1–4]. In addition, syngas is the key feedstock for various reactions such as: Fischer–Tropsch, Oxo-synthesis, methanol synthesis and etc. [5,6]. DRM process contains four reactions [7–10]:



Among these reactions, the first one is main reaction and the others are side reactions. The major problem in dry reforming of methane is deposition of produced carbon in reactions (3) and (4) [11–13]. In addition, because of endothermic nature of DRM, the reactor should work at high temperatures that lead to active phase sintering and high operational cost. In order to find a solution, various parameters such as nature of support [14,15], metal content [16,17] and addition of promoters [18,19] have been investigated. According to literature, there are two major groups of catalysts for DRM: i) Noble metal catalysts [20–22] ii) Nickel based catalysts [23–25]. From economic point of view, Nickel catalysts, especially $\text{Ni}/\text{Al}_2\text{O}_3$ is a good nominee for DRM but its problems are low resistance against severe carbon formation and phase transition of $\gamma\text{-Al}_2\text{O}_3$ to $\alpha\text{-Al}_2\text{O}_3$ at high temperatures [26]. In this regard, various promoters have been studied. It has been reported [16,26] utilizing both Mg and Al in catalyst not only increases the surface area, but also enhances the thermal stability of the catalyst. Furthermore, literature shows that addition of Mg to $\text{Ni}/\text{Al}_2\text{O}_3$ led to lower coke formation rate [27].

Apart from catalyst compositions, catalyst preparation methods have a considerable influence on the catalytic performance [28,29]. During recent decades, applying non-thermal plasma (glow discharge plasma) has received attentions due to formation of small size Ni crystals, enhancement of metal–support interaction, high dispersion of particles, increasing low-temperature activity and improving stability of catalysts [30,31].

In our continuing effort [32–34] to study the effect of argon glow discharge plasma on dry reforming of methane catalysts, $\text{Ni}/\text{MgO}-\text{Al}_2\text{O}_3$ catalyst was synthesized and the effects of plasma on coke resistance, reactivity, and structure properties were investigated. In our research impregnated $\text{Ni}/\text{MgO}-\text{Al}_2\text{O}_3$ was synthesized and treated with non-thermal plasma. Structural properties were investigated by X-ray Diffraction (XRD), Field Emission Scanning Electron Microscopy (FESEM), Transmission Electron Microscopy (TEM), Energy Dispersive X-ray (EDX Dot-Mapping), Brunauer–Emmett–Teller (BET), Thermogravimetric Analysis (TGA–DTG), X-Ray Photoelectron Spectroscopy (XPS) and Fourier Transform Infrared Spectroscopy (FTIR). Finally, activity test was done and parameters such as effect of temperature, effect of CH_4/CO_2 and effect of GHSV were investigated. In order to study catalyst activity in long-term use, stability tests were performed on both plasma treated and non-treated samples.

2. Materials and methods

2.1. Materials

In this research, $\text{Ni}(\text{NO}_3)_2 \cdot 6\text{H}_2\text{O}$ was used as nickel source and $\gamma\text{-Al}_2\text{O}_3$ powder was used as support. Moreover, $\text{Mg}(\text{NO}_3)_2 \cdot 6\text{H}_2\text{O}$ was used as promoter. All reagents purchased from Merck Company and were used without further purification. High purity methane, carbon dioxide, hydrogen and argon as plasma forming gas were purchased from Technical Gas Service in Ajman, United Arab Emirates.

2.1.1. Nanocatalyst preparation and procedures

Fig. 1 illustrates schematic flow chart of plasma treated $\text{Ni}/\text{Al}_2\text{O}_3\text{--MgO}$ (NAM-P) nanocatalyst. Generally, there are two main steps in NAM-P synthesis: (a) synthesis of support and (b) Ni addition on prepared support. In the first step, $\gamma\text{-Al}_2\text{O}_3$ and $\text{Mg}(\text{NO}_3)_2 \cdot 6\text{H}_2\text{O}$ were dissolved in de-ionized water and impregnated for 5 h at 60°C . Next, the solution was dried at 120°C for 8 h under air flow and was calcined at 600°C for 5 h. To this stage, support ($\text{Al}_2\text{O}_3\text{--MgO}$) was successfully synthesized. In next step both support and $\text{Ni}(\text{NO}_3)_2 \cdot 6\text{H}_2\text{O}$ were dissolved in de-ionized water and impregnation and drying steps procedures were the same as support synthesis. A part of synthesized sample was calcined at 600°C for 5 h and labelled as NAM-I. The other part was

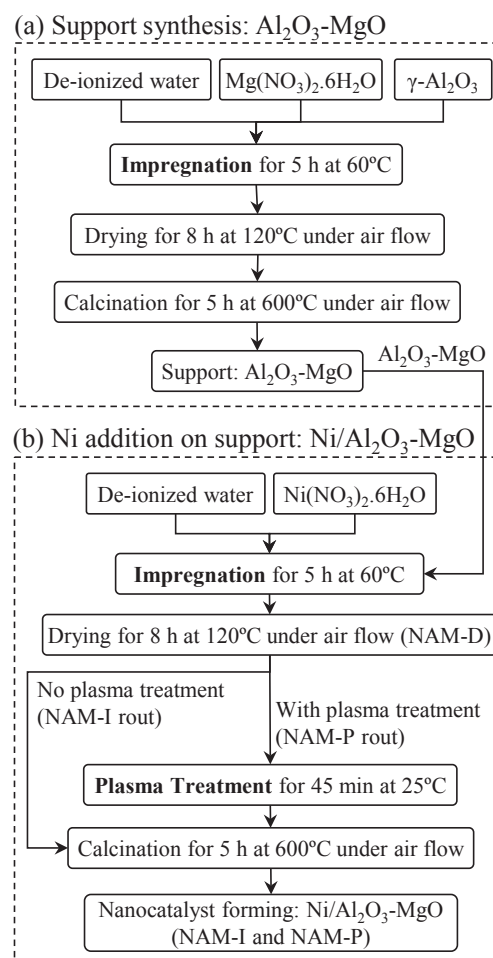


Fig. 1. Schematic flow chart for the preparation steps of $\text{Ni}/\text{Al}_2\text{O}_3\text{--MgO}$ nanocatalyst via sequential impregnation of Mg and Ni over Al_2O_3 and non-thermal plasma treatment.

exposed to glow discharge plasma for 45 min before calcination and was labelled as NAM-P. Schematic flow chart of glow discharge plasma experimental setup for treatment of Ni/Al₂O₃–MgO catalysts is illustrated in Fig. 2. In addition, a small part of sample was saved after drying step to be used at FTIR and TG–DTG analysis and was denoted as NAM-D.

2.2. Nanocatalyst characterization techniques

The structural characteristics of the catalyst was examined, using X-ray diffraction patterns in 2θ range from 20 to 90° and scanning rate of 0.02° s^{−1} by a Siemens diffractometer D5000 with monochromatized Cu-K α ($\lambda = 1.54178$ Å) radiation at 30 mA and 40 kV. The phase identification was made by comparison to Joint Committee on Powder Diffraction Standards (JCPDSs). Microstructure, particle size and morphology were investigated by field emission scanning electron microscopy (FESEM, HITACHI S-4160). To observe particle size and dispersion, transmission electron microscopy (TEM) was carried out with a Philips CM-200. Energy dispersive X-ray analysis (EDX) was carried out with a VEGA\\TESCAN equipped with a BSE detector for elemental analysis. The specific surface area (BET) of nanocatalysts was characterized by N₂ adsorption and desorption isotherms obtained at −196 °C using a Quantachrome ChemBET-3000. The thermal stability of the catalysts was determined by TGA analysis. With the PerkinElmer Thermogravimetric apparatus, the TGA analysis was performed in flowing air from room temperature to 900 °C at a heating rate of 20 °C min^{−1}. XPS was measured with a Thermo Fisher K-Alpha, equipped with a monochromatic Al K α X-ray source. Spectra were obtained using the aluminium anode (Al K $\alpha = 1486.6$ eV) operating at 150 W. Spectra were recorded at background pressure, 2×10^{-9} mbar. Binding energies were calibrated using C 1s peak at 284.5 eV. To investigate surface functional groups, Fourier Transform Infrared Spectroscopy (FTIR, UNICAM 4600) was conducted in the range of 400–4000 cm^{−1} wave numbers.

2.3. Experimental setup for catalytic performance test

The schematic of the experimental setup for activity testing of the Ni/Al₂O₃–MgO nanocatalysts for CO₂ reforming of methane is illustrated in Fig. 3. The CO₂ reforming of methane was carried out at atmospheric pressure in a 5 mm i.d. U-shape quartz tube packed bed reactor loaded with 0.1 g of the nanocatalyst layered between quartz balls. First, the nanocatalysts were reduced at 700 °C under a stream of hydrogen with a flow rate of 30 ml min^{−1} for 1 h. CH₄ and CO₂ gases were then fed into the reactor controlled by mass flow controllers (MFC, Beijing Seven star Electronics Co., Ltd.). The reactor was placed in an electrical furnace equipped with an external thermocouple placed in the middle of the nanocatalyst bed. Catalytic experiments were evaluated over the temperature range of 550–850 °C. The total flow rate was set at 40 ml min^{−1} during activity tests. The feed ratio (CH₄/CO₂) was varied from 0.5 to 2 and stability tests were performed over one day (24 h). The concentrations of the inlet and outlet gas streams were analyzed by a gas chromatograph (GC Chrom, Teif Gostar Faraz, Iran) equipped with a TCD and an FID using Plot U and Molecular Sieve columns (Agilent). The temperature of the columns was 40 °C, and Ar was used as the carrier gas. In this work, conversions of methane and carbon dioxide and also yields of hydrogen and CO were calculated according to the following formulae:

$$X_{\text{CH}_4} \% = \frac{C_{\text{CH}_4 \text{ in}} - C_{\text{CH}_4 \text{ out}}}{C_{\text{CH}_4 \text{ in}}} \times 100 \quad (5)$$

$$X_{\text{CO}_2} \% = \frac{C_{\text{CO}_2 \text{ in}} - C_{\text{CO}_2 \text{ out}}}{C_{\text{CO}_2 \text{ in}}} \times 100 \quad (6)$$

$$Y_{\text{H}_2} \% = \frac{C_{\text{H}_2 \text{ out}}}{2C_{\text{CH}_4 \text{ in}}} \times 100 \quad (7)$$

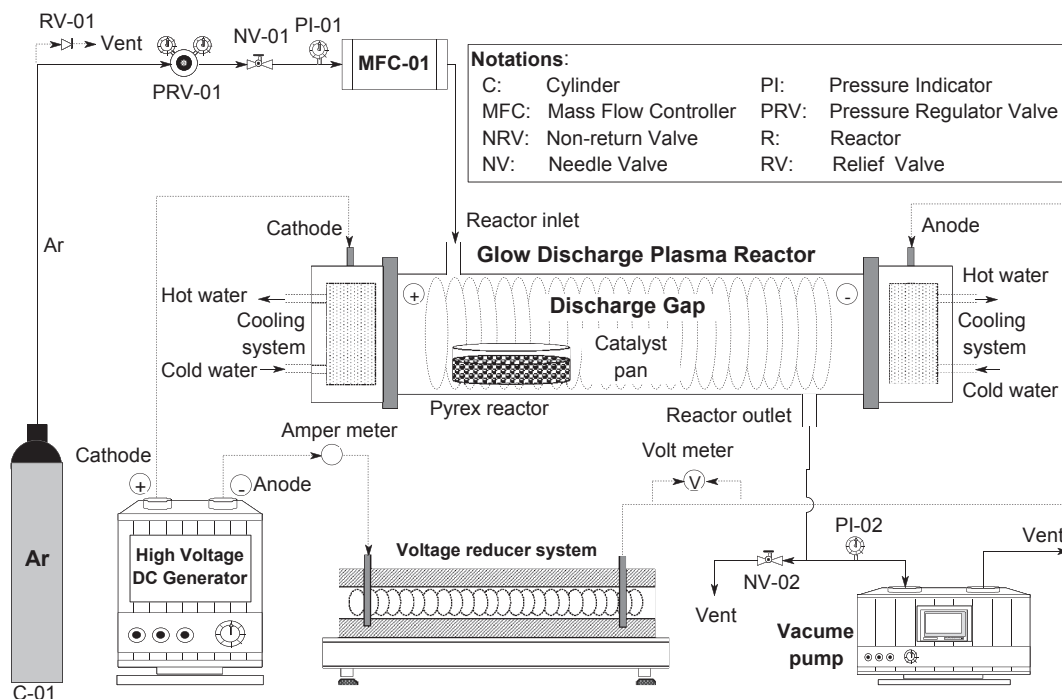


Fig. 2. Schematic flow chart of non-thermal plasma experimental setup for treatment of Ni/Al₂O₃–MgO nanocatalyst.

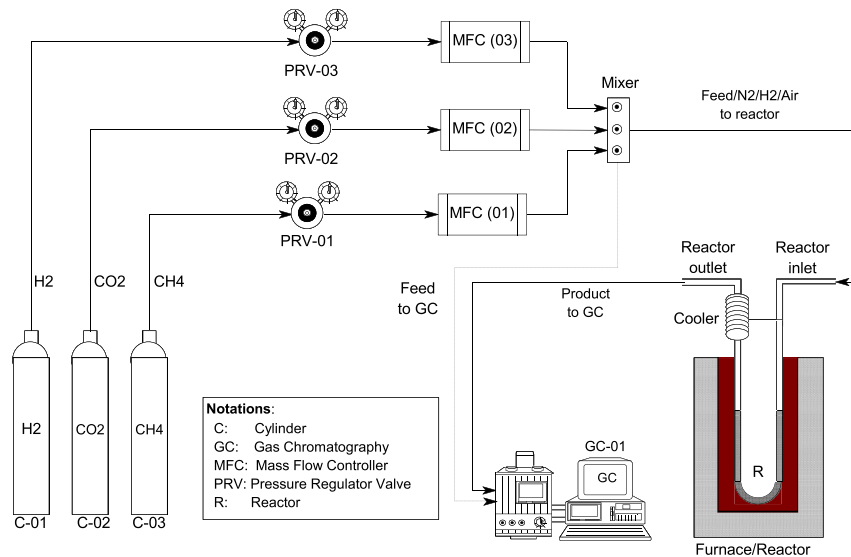


Fig. 3. Experimental setup for catalytic evaluation of Ni/Al₂O₃–MgO nanocatalyst toward hydrogen production from reforming of CH₄/CO₂ greenhouse gases.

$$Y_{\text{CO}\%} = \frac{C_{\text{CO}_{\text{out}}}}{C_{\text{CH}_4 \text{ in}} + C_{\text{CO}_2 \text{ in}}} \times 100 \quad (8)$$

where X_i and Y_i are the conversion of reactants and yields of products, respectively. $C_{i \text{ in}}$ is the initial molar fraction of component i in the feed, and $C_{i \text{ out}}$ is the final molar fraction of component i in the product stream.

3. Results and discussions

3.1. Nanocatalyst characterizations

3.1.1. XRD analysis

Fig. 4 presents XRD patterns for (a) Al₂O₃, (b) NAM-D, (c) NAM-I and (d) NAM-P samples. Concise view over patterns shows existence of γ -Al₂O₃ (00-04-0880) in cubic phase at $2\theta = 37.4, 45.8, 60.45$ and 67.3 for all samples. In addition, no peaks due to impurities were observed.

Despite similar positions for NiAl₂O₄, MgAl₂O₄ and γ -Al₂O₃ there are some differences. The main diffraction peak of γ -Al₂O₃ located at $2\theta = 67.3$ while the strongest diffraction peak for NiAl₂O₄ and MgAl₂O₄ are at $2\theta = 37.4$ [27]. In contrast, comparing γ -Al₂O₃ pattern (a) with NAM-I and NAM-P shows that the height of observed peak at $2\theta = 37.4$ becomes much higher after addition of Mg and Ni to γ -Al₂O₃. According to literature, this observation confirms existence of NiAl₂O₄ (00-010-0339) and maybe formation of MgAl₂O₄ (00-001-1157) in cubic phase in the catalyst structure [27]. In addition, a comparison between patterns (b) with patterns (c) and (d) reveals that most of the peaks become higher after calcination, but the height of diffraction peak at $2\theta = 37.4$ has become much higher than the others. This observation is another reason for formation of NiAl₂O₄ spinels after calcination. It has been reported NiAl₂O₄ forms in Ni/ γ -Al₂O₃ catalyst after calcination at 550 °C [27]. In the case of NiO (01-073-1519), it seems that there are small peaks at $2\theta = 19.1, 31.4, 37.0, 45.0, 59.7$ and 65.5 . The low height of the peak might be due to transformation of most of NiO phase to NiAl₂O₄ or high dispersion of NiO [35]. High dispersion of active phase could be the result of high interaction between Ni and Mg and/or Al. There is no sign of NiO formation in NAM-D sample and it shows higher temperature is necessary to form NiO.

3.1.2. FESEM analysis

Fig. 5 depicts FESEM micrographs and particle size distribution of (a) γ -Al₂O₃, (b) impregnated Ni/Al₂O₃–MgO and (c) plasma treated Ni/Al₂O₃–MgO. A general view over figures reveals that in comparison with γ -Al₂O₃ more uniform pattern has formed in both NAM-I and NAM-P. A comparison between micrographs (b) and (c) shows decreasing of number of agglomerations and small particles after plasma treatment. In addition, it seems that all of the nanocatalyst particles in NAM-P are flattered on the surface of the

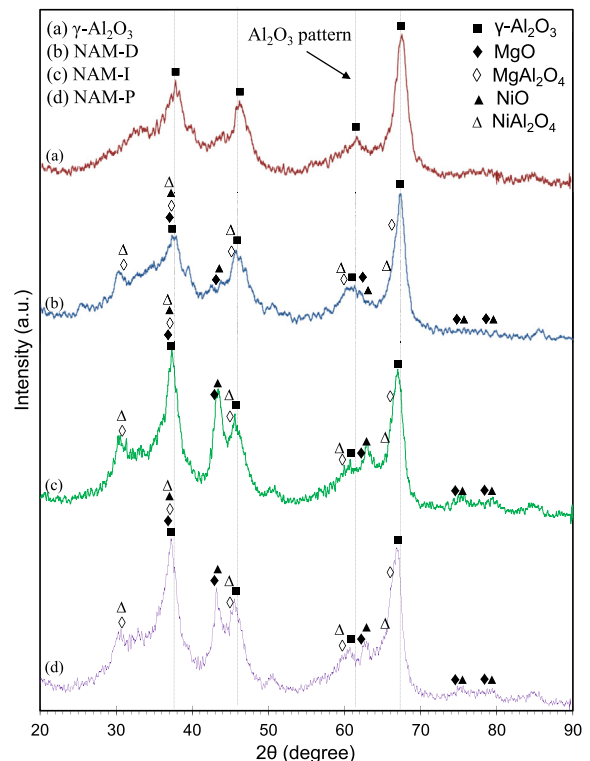


Fig. 4. XRD patterns of (a) γ -Al₂O₃ and Ni/Al₂O₃–MgO nanocatalysts: (b) NAM-D (c) NAM-I and (d) NAM-P.

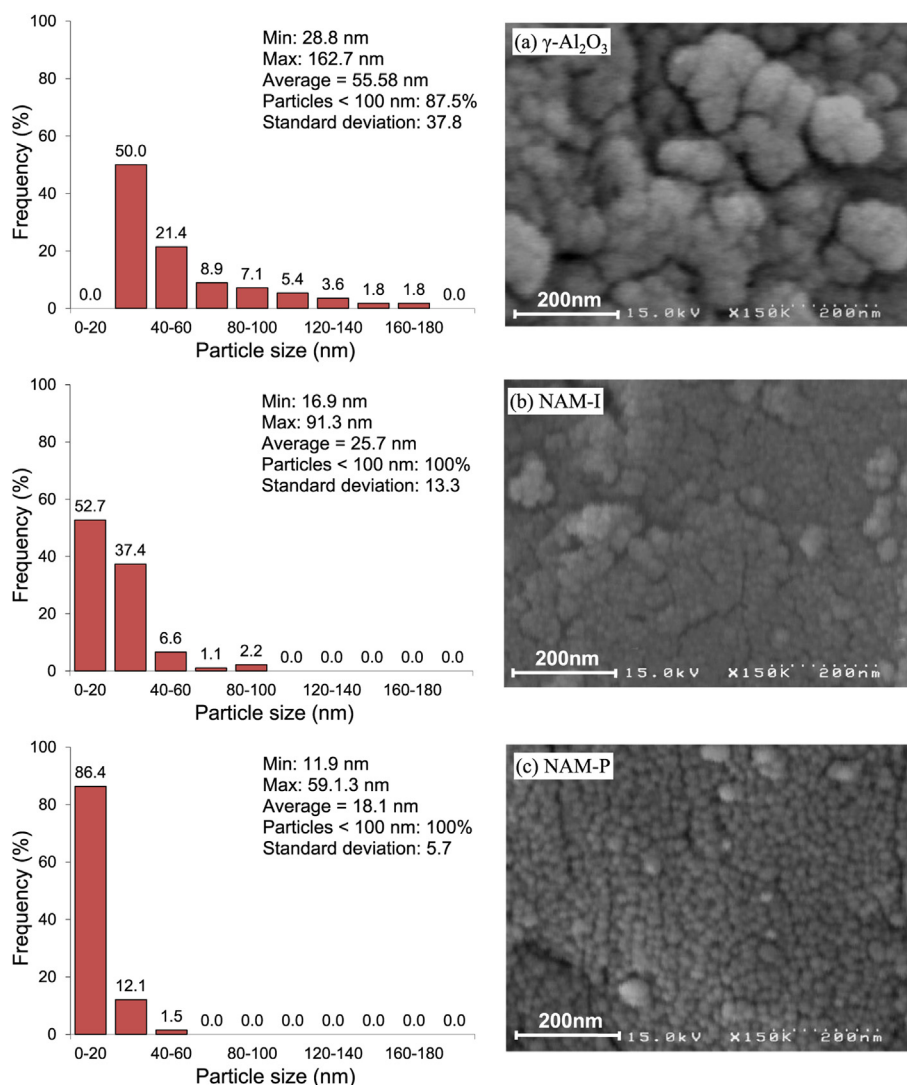


Fig. 5. FESEM images and particle size histogram of (a) γ -Al₂O₃ and Ni/Al₂O₃–MgO nanocatalysts: (b) NAM-I and (c) NAM-P.

support; thus, mass transport limitations will probably become lower for the NAM-P nanocatalyst. Therefore, it is expected that the reactants easily adsorb and react on the surface of the plasma treated nanocatalyst. This observation is in complete agreement with our previous works [32–34,36].

Particle size distribution analysis shows that in the case of γ -Al₂O₃, 50% of particles are in 20–40 nm range and average particle size is 55.58 nm while for NAM-I 52.7% particles are in 20–40 nm and average particle size is 25.7 nm which is less than a half of reported particle size for γ -Al₂O₃. Moreover, third particle size histogram reveals that after plasma treatment 86.4% of particles are in 20–40 nm range and average particle size is 18.1 nm. Investigating particle size histograms represents significant effect of utilizing glow discharge plasma in catalyst preparation. Glow discharge plasma contains radicals, ions, energetic electrons and neutral particles. These energetic particles and ions could modify particle size and destruct agglomerations which enhance stability and activity of the catalyst [37–39].

3.1.3. TEM analysis

Fig. 6 displays TEM analysis and active phase particle size histogram of plasma treated Ni/Al₂O₃–MgO nanocatalyst. A

general view over the figure reveals small particles with uniform dispersion for NAM-P. These observations demonstrate the advantages of utilizing plasma in preparation step. Tang et al. [40] reported 10 nm and Kim et al. [41] reported 7 nm as critical particle sizes for CO₂ reforming below which carbon deposition can be avoided. These obtained results can be used to interpret the observations from particle size histogram of NAM-P. The histogram shows formation of particles with average size of 7.3 nm. In addition, 58.6% of particles are in 5–10 nm range and 22% are <5 nm and minimum and maximum analysed Ni particle sizes are 1.5 and 24.6 nm respectively. According to mentioned above, NAM-P is expected to be a stable catalyst in CO₂ reforming of methane process.

3.1.4. EDX dot-mapping analysis

In order to confirm the presence of different components and also, distribution of the desirable elements in the nano composite structure, qualitative elemental analysis was performed by EDX dot-mapping. EDX dot-mapping analysis of plasma treated Ni/Al₂O₃–MgO is illustrated in Fig. 7. This figure confirms existence of Ni, Al and Mg in catalyst structure. According to Fig. 7, Ni is highly dispersed over support. In addition there is a uniform pattern for

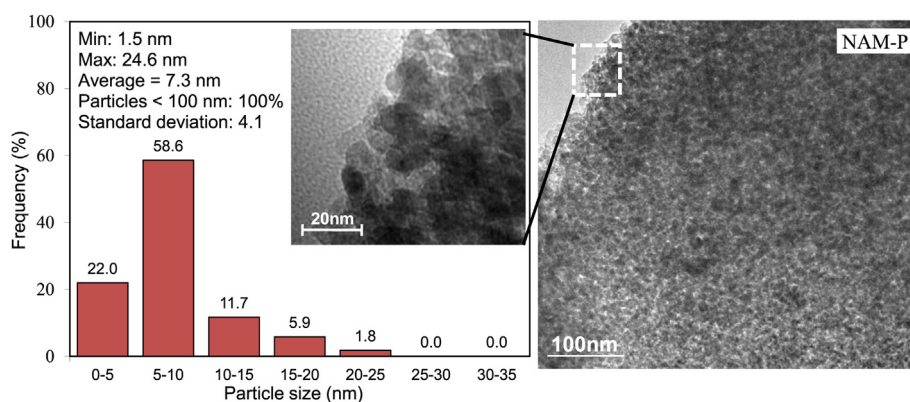


Fig. 6. TEM image and active phase particle size histogram of Ni/Al₂O₃–MgO nanocatalyst treated with non-thermal plasma (NAM-P).

Mg. No sintering or particle growth was observed in Ni particles, which is in complete agreement with XRD results. To sum up, EDX revealed significant effect of plasma treatment on dispersion of active phase over the support.

3.1.5. BET analysis

The calculated surface areas for γ -Al₂O₃, NAM-D, NAM-I and NAM-P are shown in Fig. 8. The results show 41.1, 69.8, 78.5 and 116 m² g^{−1} for, NAM-D, NAM-I, NAM-P and γ -Al₂O₃. The surface of γ -Al₂O₃ is 32% more than NAM-P and 40% more than NAM-I. Utilizing MgO and Ni in catalyst structure cause reduction in surface area. The other reason might be agglomeration of metal particles after metal decomposition and plugging the pores of the support. According to FESEM and TEM images, the number of agglomerations in NAM-I is more than NAM-P. In addition, plasma enhances the surface area by making smaller particles. According to mentioned above, we expected higher surface area for NAM-P in comparison with NAM-I. As expected, NAM-P has ca. 11% higher surface than NAM-I. Higher surface area helps the accessibility of reactant to active sites [37]. Also, higher surface area can decrease coke formation and enhance adsorption of CO₂ [42].

3.1.6. TG–DTG analysis

Fig. 9 reveals TG–DTG analysis of Ni/Al₂O₃–MgO nanocatalyst for (a) NAM-D, (b) NAM-I and (c) NAM-P samples. This analysis is

usually used to examine thermal stability of prepared nanocatalyst. A general view over figure shows four major zones between 0 and 200, 200–300, 300–500 and 500–800 °C in TG profiles. As it can be deduced from Fig. 9:

- The physically adsorbed water was eliminated below 200 °C. Desorption of hydroxyl groups led to ca. 11% weight loss in NAM-D [43,44].
- In temperature range of 200–300 °C, there is a rapid slope in TG curve (a). The considerable weight loss can be attributed to elimination of nitrate groups that existed in Ni(NO₃)₂·6H₂O and Mg(NO₃)₂·6H₂O in preparation step.
- In second zone there is ca. 8% weight loss for NAM-D while there are no considerable weight loss for NAM-I and NAM-P. This observation proves desorption of nitrate groups after calcination.
- The third zone between 300 and 500 °C shows ca. 5% weight loss for non-calcined sample. The weight loss can be assigned to loss of physisorbed CO₂ or other impurities in preparation step or during thermogravimetric test. This weight loss can be attributed to NiO formation.
- In last zone there are no significant weight loss which shows all nitrates and adsorbed water have been eliminated from nanocatalyst and this temperature range is a suitable range for setting as calcination temperature.

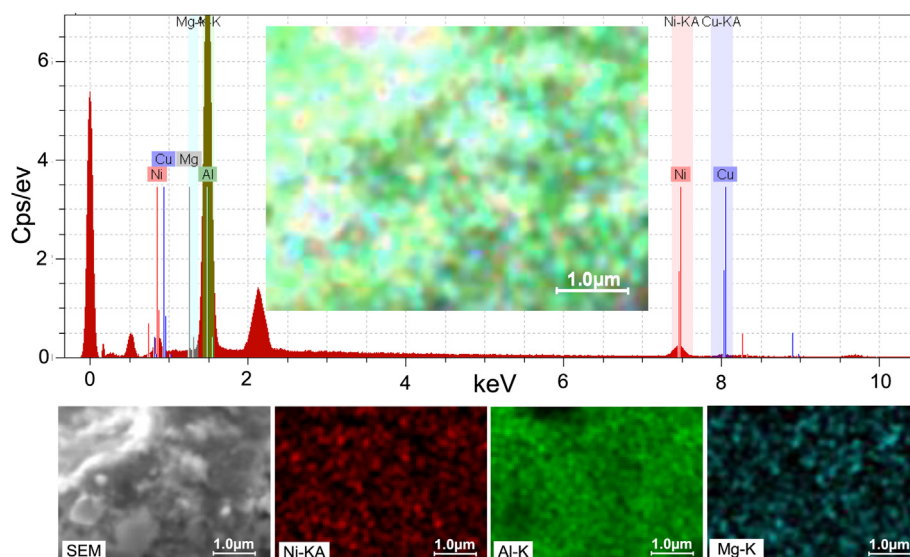


Fig. 7. EDX dot-mapping analysis of Ni/Al₂O₃–MgO nanocatalyst treated with non-thermal plasma (NAM-P).

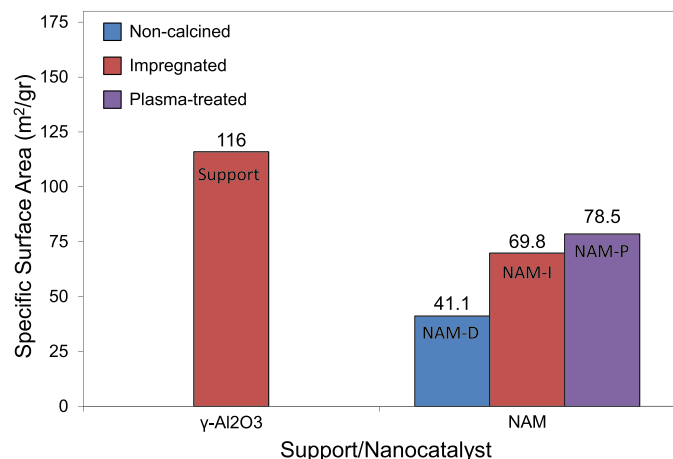


Fig. 8. BET surface area analysis of Al₂O₃ and Ni/Al₂O₃-MgO nanocatalysts: NAM-D, NAM-I and NAM-P.

3.1.7. XPS analysis

Fig. 10 reveals Ni 2p_{3/2} and Al 2p XPS spectra of NAM-I and NAM-P nanocatalysts. A general view over Fig. 10 shows no significant change in peak positions. This means Ni species are in the same state in all samples. The overall Ni 2p_{3/2} peak at binding energy of 856.0 eV is accompanied by a shake-up satellite peak at 861.8 eV in all samples. The observed peak at 856.0 eV is deconvoluted to two peaks. This observation means Ni exists in two states: 1. Ni at 854 eV, 2. NiAl₂O₄ at 856 eV. This is completely consistent with XRD results. As observed in the XPS spectra NiAl₂O₄/NiO ratio is higher for NAM-P nanocatalyst which shows existence of more amount of NiAl₂O₄ in the structure of plasma treated sample. Higher amount of NiAl₂O₄ reveals higher interaction between Ni and support particles which will have direct effect on improved stability of the plasma treated catalyst. Comparing amount of Ni/Al ratio (0.039 versus 0.126 for plasma treated NAM-I and NAM-P respectively) also shows higher amount of this ratio for NAM-P catalyst which shows higher dispersion of Ni over support.

3.1.8. FTIR analysis

FTIR spectrums of (a) γ-Al₂O₃, (b) NAM-D, (c) NAM-I and (d) NAM-P are shown in Fig. 11. There are no considerable changes in

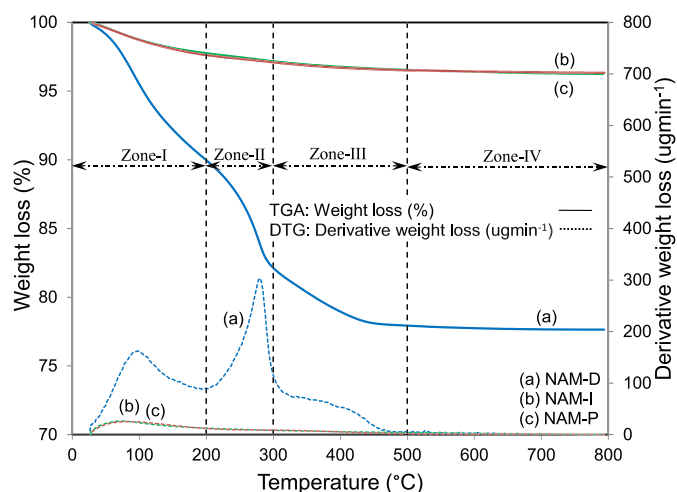


Fig. 9. TG-DTG analysis of Ni/Al₂O₃-MgO nanocatalysts: (a) NAM-D, (b) NAM-I and (c) NAM-P.

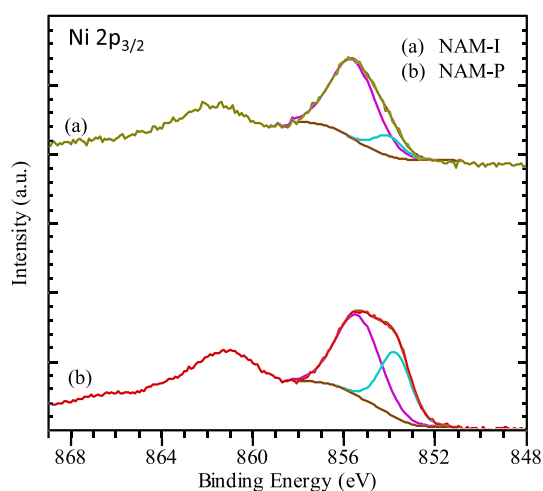
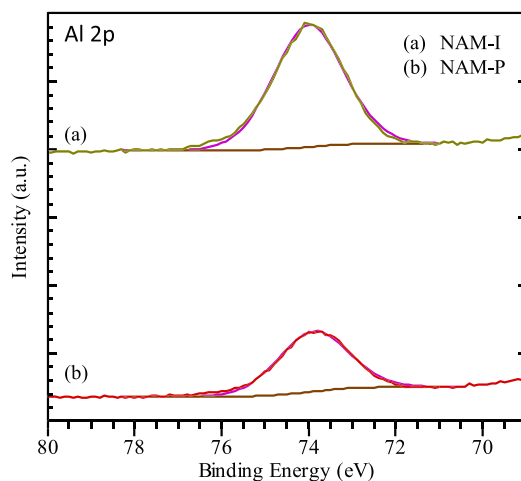


Fig. 10. XPS analysis of Ni/Al₂O₃-MgO nanocatalysts: (a) NAM-I and (b) NAM-P.

peak positions but it seems recorded peaks for NAM-P are more intense than NAM-I that confirm more structured-form of plasma treated nanocatalyst. There are six main peaks in spectrums at: 530, 710, 1400, 1649, 2370 and 3450 cm⁻¹. The broad peak at 3450 cm⁻¹ is attributed to interacting OH [45] or to bridging OH groups [46]. The peak at 1649 cm⁻¹ is assigned to the O-H bending vibrating mode of the interlayer water molecules, which are associated with the adsorbed water on the products [47]. Recorded peak at 2370 cm⁻¹ is related to the C-H stretching mode of atmospheric hydrocarbons on the surface of the nanocatalysts [48]. A comparison between spectrums (b) with (c) and (d) shows the peaks at 3450 and 1649 cm⁻¹ are more intense at NAM-D. This observation reveals the positive effect of calcination step in water desorption from nanocatalyst structure. The other adsorption peaks below 800 cm⁻¹ are attributed to metal oxides arising from inter-atomic vibrations [49,50].

3.2. Catalytic performance study toward reforming of CH₄/CO₂

3.2.1. Effect of plasma treatment

Fig. 12 depicts the effect of temperature on the H₂ and CO yields for NAM-I and NAM-P nanocatalysts. The figure shows that in all temperatures H₂ and CO yields for NAM-P are always higher than NAM-I. Moreover, by increasing reaction temperature CH₄ conversion and consequently CO and H₂ yield in both catalysts increased which is in consistent with the results in other literature [51]. In

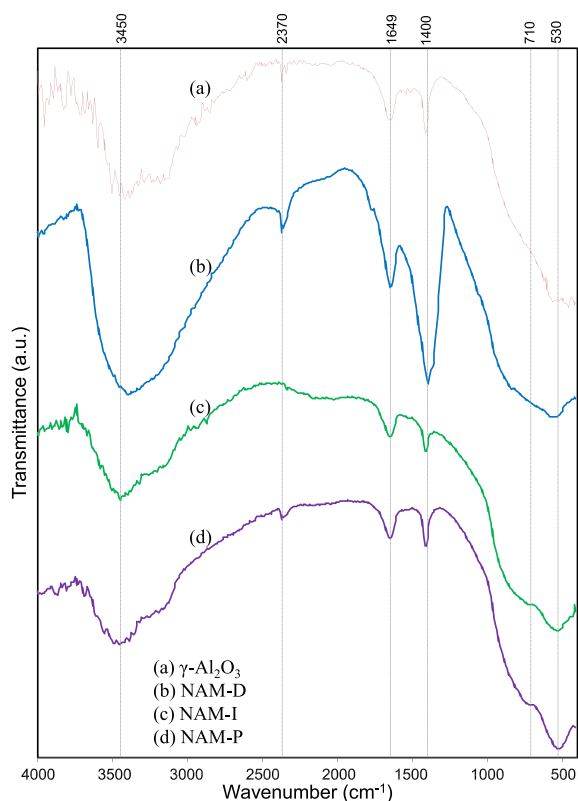


Fig. 11. FTIR spectra of (a) γ - Al_2O_3 and $\text{Ni}/\text{Al}_2\text{O}_3$ – MgO nanocatalysts: (b) NAM-D (c) NAM-I and (d) NAM-P.

addition, CO yield is always more than H_2 yield. Generally, NAM-P is more successful to convert CO_2 and CH_4 to H_2 and CO. According to characterizations, improved morphology of the catalyst and utilizing glow discharge plasma in preparation step have led to high performance of NAM-P.

Apart from utilizing glow discharge plasma in preparation step, using MgO in catalyst structure shows a significant activity in comparison with the other similar catalysts. Comparison between the obtained yields for NAM-I with impregnated $\text{Ni}/\text{Al}_2\text{O}_3$ catalyst [33] shows that NAM-I has 10% higher CO yield at

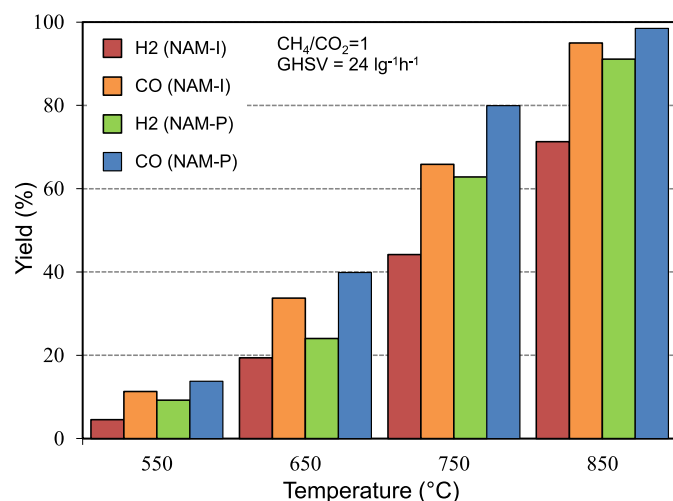


Fig. 12. Effect of temperature on H_2 and CO yields over NAM-I and NAM-P nanocatalysts.

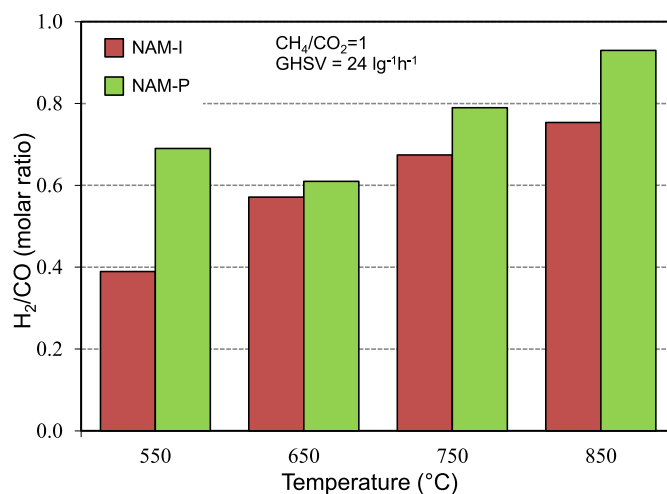


Fig. 13. Effect of temperature on H_2/CO molar ratio produced over NAM-I and NAM-P nanocatalysts.

850°C under the same reaction conditions. Also, investigated $\text{Ni}/\text{Al}_2\text{O}_3$ – ZrO_2 [32] catalyst with the similar preparation and reaction condition reaches approximately 84% and 60% yield for CO and H_2 respectively. According to Fig. 12, the yield of NAM-I is 10% more in terms of H_2 and CO in comparison with $\text{Ni}/\text{Al}_2\text{O}_3$ – ZrO_2 .

Fig. 13 shows effect of temperature on H_2/CO molar ratio produced over NAM-I and NAM-P nanocatalysts. H_2/CO ratio is a key parameter in produced syngas via DRM. In addition, investigation of H_2/CO ratio is an important factor for showing the selectivity of catalyst. The figure reveals that at all of the temperatures H_2/CO molar ratio is higher for NAM-P due to well-dispersed active phase and higher active surface area. For both samples H_2/CO ratio is below 1 at all reaction temperatures. This observation demonstrates consumption of hydrogen due to the reverse water gas shift (RWGS) reaction. H_2/CO molar ratio reaches more than 0.9 for NAM-P while for NAM-I the ratio is ca. 0.75.

3.2.2. Effect of CH_4/CO_2 in feed

Fig. 14 depicts effect of CH_4/CO_2 in feed on H_2 and CO yields over NAM-I and NAM-P nanocatalyst. As can be seen, increasing CH_4/CO_2

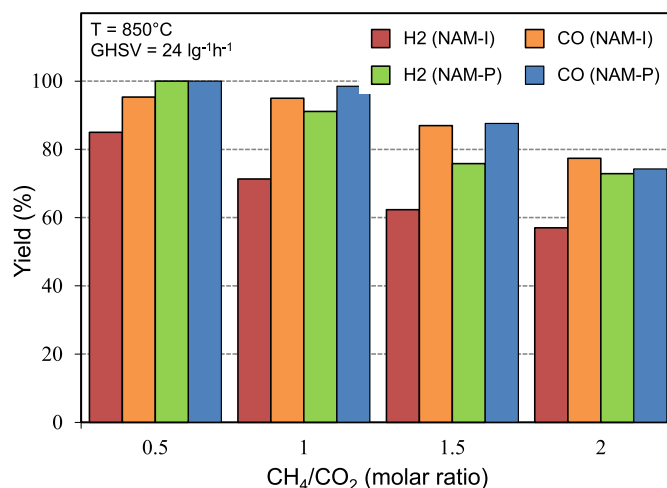


Fig. 14. Effect of CH_4/CO_2 in feed on H_2 and CO yields produced over NAM-I and NAM-P nanocatalysts.

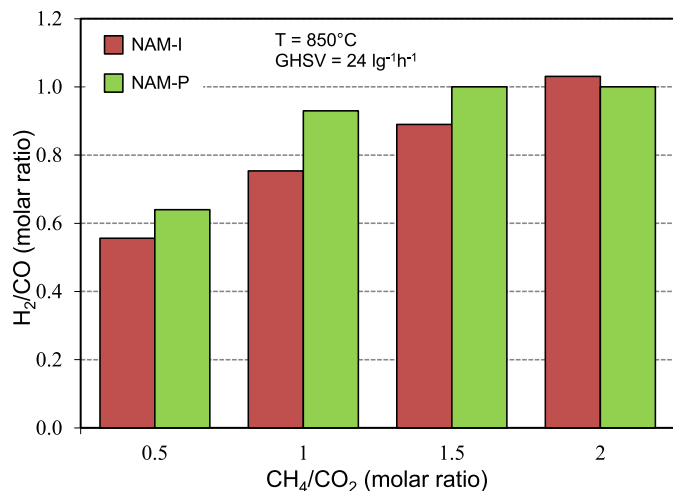


Fig. 15. Effect of CH₄/CO₂ in feed on H₂/CO molar ratio produced over NAM-I and NAM-P nanocatalysts.

ratio leads to decreasing product yield. As expected, plasma treated sample is more active at 0.5–1.5 CH₄/CO₂ ratios. As CH₄/CO₂ ratio enhances, the H₂ and CO yields decrease significantly. By raising the CH₄/CO₂ ratio in the feed, H₂ consumption resulting from RWGS reaction is suppressed due to unavailability of CO₂. Nevertheless, increasing the CH₄/CO₂ ratio leads to the raising of H₂/CO ratio, but products yield decrease and the difference between reactants conversion increase. The effect of CH₄/CO₂ in feed on H₂/CO molar ratio is shown in Fig. 15. In comparison with NAM-I, NAM-P is more active in CO and H₂ production. At higher CH₄/CO₂ ratios coke will create rapidly [52,53]. More coke deposition means less H₂ and CO yield.

3.2.3. Effect of GHSV

In order to investigate the potential of catalysts to be used in industrial scales, it is crucial to study parameters such as GHSV. Fig. 16 depicts effect of GHSV in terms of H₂ and CO yields for NAM-I and NAM-P. The yields of CO and H₂ decrease by increasing GHSV for both samples. Higher GHSV means higher space velocity of the feed and it results in less residence time. As the contact time between feed molecules and catalyst surface decreases, CH₄ and CO₂

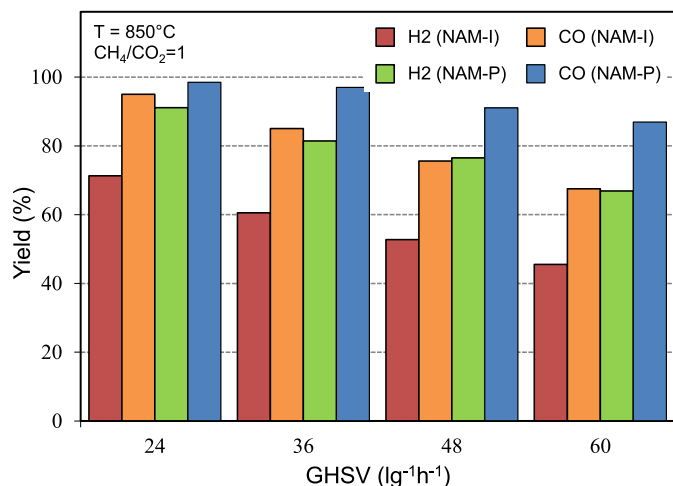


Fig. 16. Effect of GHSV on H₂ and CO yields produced over NAM-I and NAM-P nanocatalysts.

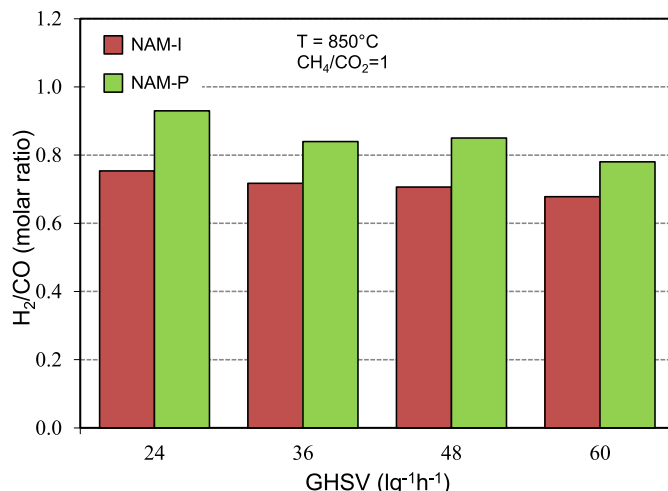


Fig. 17. Effect of GHSV on H₂/CO molar ratio produced over NAM-I and NAM-P nanocatalysts.

are not able to interact with the active Ni particles inside the nanocatalyst pores. Thus, some of the feed remains unreacted. However, Fig. 16 reveals that NAM-P has higher activity in high GHSVs in comparison with NAM-I.

Fig. 17 depicts effect of GHSV on H₂/CO molar ratio over NAM-I and NAM-P. As expected, the figure shows increasing H₂/CO ratio by increasing GHSV and also H₂/CO < 1 for both samples because of H₂ consumption at Reverse Water Gas Shift (RWGS) reaction. At all of the GHSVs H₂/CO ratio is higher for NAM-P due to well-dispersed small particle size for plasma treated sample. A GHSV = 60 l g⁻¹ h⁻¹ H₂/CO is ca. 0.8 for NAM-P while this ratio is ca. 0.7 for NAM-I.

3.2.4. Time on stream performance

Time on stream performance test for 1440 min was performed at 850 °C for both NAM-I and NAM-P and the results are shown in Fig. 18. A general view over figure reveals that in 850 °C, NAM-P has more conversion in terms of H₂ and CO yields. Fig. 18 shows NAM-P is stable while there is a considerable reduction in stability of NAM-I in H₂ yield. It has been reported that [8], carbon formation is the main reason of catalysts deactivation in CO₂ reforming. On the other words, carbon species can be created when the rate of reactions which lead to carbon formation is higher than carbon

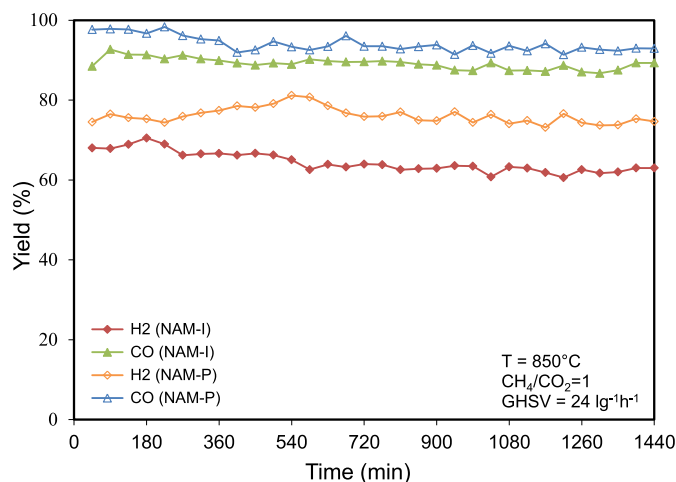


Fig. 18. Time on stream performance of NAM-I and NAM-P nanocatalysts in terms of H₂ and CO yields.

elimination rate. Deposition of carbon deactivates catalyst in two ways:

- Removing carbon from surface
- Encapsulating carbon or diffusing through the Ni after dissolving [54]

Generally, controlling the size of metal atom ensembles on the surface, as observed in NAM-P nanocatalyst, would be very helpful to decrease or inhibit carbon deposition. High dispersion of Ni particles and also small Ni particle size that was obtained from utilizing glow discharge plasma decrease structure defects and reduce the tendency of carbon to attach or diffuse into Ni particles [55]. According to above mentioned, long-term stability of NAM-P in comparison with NAM-I can be attributed to anti-coke formation nature of catalyst.

The other reason of NAM-P high stability can be addressed by EDX. High distribution of Mg increases the number of oxidant sites for NAM-P nanocatalyst. In addition, good dispersion of Ni particles due to existence of MgO that avoids sintering of Ni nano particles is the other reason for long-term stability of both catalysts.

4. Conclusions

In the present work, Ni/Al₂O₃–MgO was synthesized and the effect of glow discharge plasma on the structure, reactivity and stability of the catalyst was studied. The beneficial effect of utilizing plasma was proved on physicochemical properties of Ni/Al₂O₃–MgO nanocatalyst. According to characterization results, XRD did not show any impurities in the synthesized samples. FESEM revealed smaller particle size (Average = 18.1 nm) for plasma treated sample. TEM and EDAX proved a uniform dispersion of metals in plasma treated catalyst. According to BET, 11% higher specific surface area for plasma treated sample was obtained. In addition, activity test revealed the significant effect of glow discharge plasma on catalyst. Much better low-temperature activity, higher H₂/CO ratio, high potential to convert CO₂ and CH₄ to products at high GHSVs and significant stability for plasma treated sample in comparison with the conventional impregnation sample were observed. According to effectiveness and novelty of glow discharge plasma for catalytic purposes, further studies to develop ways for commercializing plasma technology in synthesis and post-treatment of nanocatalysts are recommended.

Acknowledgements

The authors gratefully acknowledge National Iranian Oil Refining and Distribution Company for the financial support of the research under project number of 87-1037 as well as Sahand University of Technology and Iran Nanotechnology Initiative Council for complementary financial supports.

References

- [1] M.C.J. Bradford, M.A. Vannice, *Appl. Catal. A* 142 (1996) 73–96.
- [2] Z.X. Cheng, X.G. Zhao, J.L. Li, Q.M. Zhu, *Appl. Catal. A* 205 (2001) 31–36.
- [3] B. Fidalgo, A. Domínguez, J.J. Pis, J.A. Menéndez, *Int. J. Hydrogen Energy* 33 (2008) 4337–4344.
- [4] S. Zeng, L. Zhang, X. Zhang, Y. Wang, H. Pan, H. Su, *Int. J. Hydrogen Energy* 37 (2012) 9994–10001.
- [5] C. Crisafulli, S. Scirè, S. Minicò, L. Solarino, *Appl. Catal. A* 225 (2002) 1–9.
- [6] R. Martínez, E. Romero, C. Guimon, R. Bilbao, *Appl. Catal. A* 274 (2004) 139–149.
- [7] M. Haghighi, Z.-q. Sun, J.-h. Wu, J. Bromly, H.L. Wee, E. Ng, Y. Wang, D.-k. Zhang, *Proc. Combust. Inst.* 31 (2007) 1983–1990.
- [8] S.M. Sajjadi, M. Haghighi, A. Alizadeh Eslami, F. Rahmani, *J. Sol–Gel Sci. Technol.* 67 (2013) 601–617.
- [9] S. Aghamohammadi, M. Haghighi, S. Karimipour, *J. Nanosci. Nanotechnol.* 13 (2013) 4872–4882.
- [10] C. Guerra, A. Lanzini, P. Leone, M. Santarelli, N.P. Brandon, *J. Power Sources* 245 (2014) 154–163.
- [11] F. Guo, Y. Zhang, G. Zhang, H. Zhao, *J. Power Sources* 231 (2013) 82–90.
- [12] A. Kaengsilalai, A. Luengnaruemitchai, S. Jitkarnka, S. Wongkasemjit, *J. Power Sources* 165 (2007) 347–352.
- [13] G. Valderrama, A. Kiennemann, M.R. Goldwasser, *J. Power Sources* 195 (2010) 1765–1771.
- [14] J.D.A. Bellido, E.M. Assaf, *Appl. Catal. A* 352 (2009) 179–187.
- [15] L.B. Råberg, M.B. Jensen, U. Olsbye, C. Daniel, S. Haag, C. Mirodatos, A.O. Sjøstad, *J. Catal.* 249 (2007) 250–260.
- [16] J. Zhang, H. Wang, A.K. Dalai, *J. Catal.* 249 (2007) 300–310.
- [17] E. Ruckenstein, Y. Hang Hu, *J. Catal.* 162 (1996) 230–238.
- [18] M. Ghelamallah, P. Granger, *Fuel* 97 (2012) 269–276.
- [19] A. Horváth, G. Stefler, O. Geszti, A. Kiennemann, A. Pietraszek, L. Gucci, *Catal. Today* 169 (2011) 102–111.
- [20] F. Pompeo, N.N. Nichio, M.G. González, M. Montes, *Catal. Today* 107–108 (2005) 856–862.
- [21] J.R.H. Ross, *Catal. Today* 100 (2005) 151–158.
- [22] S. Wang, G.Q.M. Lu, *Appl. Catal. B* 16 (1998) 269–277.
- [23] M.M. Barroso-Quiroga, A.E. Castro-Luna, *Int. J. Hydrogen Energy* 35 (2010) 6052–6056.
- [24] M. Ocsachoque, F. Pompeo, G. Gonzalez, *Catal. Today* 172 (2011) 226–231.
- [25] K.-M. Kang, H.-W. Kim, I.-W. Shim, H.-Y. Kwak, *Fuel Process. Technol.* 92 (2011) 1236–1243.
- [26] Y. Qiu, J. Chen, J. Zhang, *J. Nat. Gas Chem.* 16 (2007) 148–154.
- [27] Y. Qiu, J. Chen, J. Zhang, *Front. Chem. Eng. China* 1 (2007) 167–171.
- [28] P. Estifae, M. Haghighi, N. Mohammadi, F. Rahmani, *Ultrason. Sonochem.* 21 (2014) 1155–1165.
- [29] F. Rahmani, M. Haghighi, P. Estifae, *Microporous Mesoporous Mater.* 185 (2014) 213–223.
- [30] C.-j. Liu, K. Yu, Y.-p. Zhang, X. Zhu, F. He, B. Eliasson, *Appl. Catal. B* 47 (2004) 95–100.
- [31] Y.-P. Zhang, P.-S. Ma, X. Zhu, C.-j. Liu, Y. Shen, *Catal. Commun.* 5 (2004) 35–39.
- [32] N. Rahemi, M. Haghighi, A.A. Babaluo, M. Jafari Fallah, P. Estifae, *J. Ind. Eng. Chem.* 19 (2013) 1566–1576.
- [33] N. Rahemi, M. Haghighi, A.A. Babaluo, M. Fallah Jafari, P. Estifae, *J. Nanosci. Nanotechnol.* 13 (2013) 4896–4908.
- [34] N. Rahemi, M. Haghighi, A.A. Babaluo, M. Fallah Jafari, P. Estifae, *Plasma Chem. Plasma Process.* 33 (2013) 663–680.
- [35] J. Zhang, H. Wang, A.K. Dalai, *Appl. Catal. A* 339 (2008) 121–129.
- [36] N. Rahemi, M. Haghighi, A.A. Babaluo, M. Fallah Jafari, S. Khorram, *J. Appl. Phys.* 114 (2013) 0943011–09430110.
- [37] K.-S. Hwang, H.Y. Zhu, G.Q. Lu, *Catal. Today* 68 (2001) 183–190.
- [38] J. Kaspar, P. Fornasiero, M. Graziani, *Catal. Today* 50 (1999) 285–298.
- [39] Z.-j. Wang, Y. Zhao, L. Cui, H. Du, P. Yao, C.-j. Liu, *Green Chem.* 9 (2007) 554–559.
- [40] S. Tang, L. Ji, J. Lin, H.C. Zeng, K.L. Tan, K. Li, *J. Catal.* 194 (2000) 424–430.
- [41] J.-H. Kim, D.J. Suh, T.-J. Park, K.-L. Kim, *Appl. Catal. A* 197 (2000) 191–200.
- [42] Z. Hou, T. Yashima, *Appl. Catal. A* 261 (2004) 205–209.
- [43] A.M. Gadalla, H.-F. Yu, *J. Therm. Anal.* 37 (1991) 319–331.
- [44] J.S. Gnanaraj, V.G. Pol, A. Gedanken, D. Aurbach, *Electrochem. Commun.* 5 (2003) 940–945.
- [45] S. Lacombe, C. Geantet, C. Mirodatos, *J. Catal.* 151 (1995) 439–452.
- [46] X.E. Verykios, *Int. J. Hydrogen Energy* 28 (2003) 1045–1063.
- [47] P. Jeevanandam, Y. Koltypin, A. Gedanken, *Mater. Sci. Eng. B* 90 (2002) 125–132.
- [48] K. Anandan, V. Rajendran, *Mater. Sci. Semicond. Process.* 14 (2011) 43–47.
- [49] O. Mabayoje, M. Seredych, T.J. Bandoz, *J. Colloid Interface Sci.* 378 (2012) 1–9.
- [50] J. Taghavi Moghaddam, G.P. Knowles, A.L. Chaffee, *J. Mol. Catal. A Chem.* 358 (2012) 79–88.
- [51] S. Pengpanich, V. Meeyoo, T. Rirksomboon, *Catal. Today* 93–95 (2004) 95–105.
- [52] J.H. Edwards, A.M. Maitra, *Fuel Process. Technol.* 42 (1995) 269–289.
- [53] A.M. Gadalla, B. Bower, *Chem. Eng. Sci.* 43 (1988) 3049–3062.
- [54] V.C.H. Kroll, H.M. Swaan, C. Mirodatos, *J. Catal.* 161 (1996) 409–422.
- [55] D. Chen, K.O. Christensen, E. Ochoa-Fernández, Z. Yu, B. Tødtal, N. Latorre, A. Monzón, A. Holmen, *J. Catal.* 229 (2005) 82–96.